Accurate In Vivo Nanothermometry through NIR-II Lanthanide Luminescence Lifetime

Meiling Tan[1,2,3], Feng Li[1,2,3], Ning Cao[4], Hui Li[1,2,3], Xin Wang[1,2,3], Chenyang Zhang[1,2,3], Daniel Jaque[5], and Guanying Chen[1,2,3*]

[1]MIIT Key Laboratory of Critical Materials Technology for New Energy Conversion and Storage, School of Chemistry and Chemical Engineering, Harbin Institute of Technology, 150001 Harbin, People's Republic of China.
[2]Key Laboratory of Micro-systems and Micro-structures, Ministry of Education, Harbin Institute of Technology, 150001 Harbin, People's Republic of China
[3]State Key Laboratory of Urban Water Resource and Environment, School of Chemistry and Chemical Engineering, Harbin Institute of Technology, Harbin 150001, People's Republic of China.
[4]Department of Learning and Instruction, University at Buffalo, State University of New York, Buffalo, NY 14260, USA
[5]Fluorescence Imaging Group, Universidad Autonoma de Madrid, Madrid 28049, Spain
*Correspondence: chenguanying@hit.edu.cn

Abstract: Luminescence nanothermometry is promising for non-invasive probing of temperature in biological microenvironment at nanometric spatial resolution. Yet, wavelength- and temperature-dependent absorption and scattering of tissues distort measured luminescence spectral profile, rendering conventional luminescence nanothermometers (ratiometric, intensity, band shape, or spectral shift) problematic for *in vivo* temperature determination. Here, we describe a class of lanthanide-based nanothermometers, which are able to provide precise and reliable temperature readouts at varied tissue depths through NIR-II luminescence lifetime. To achieve this, we have devised an inert core /active shell/inert shell structure of tiny nanoparticles (size, 13.5 nm), in which thermosensitive lanthanide ion pairs (ytterbium and neodymium) are spatially confined in the thin middle shell layer (sodium yttrium fluoride, 1 nm), ensuring being homogenously close to the surrounding environment while meanwhile protected by the outmost calcium fluoride shell (CaF_2, ~ 2.5 nm) that shields out bioactive milieu interferences. This ternary structure endows the nanothermometers with the ability to consistently resolve temperature changes at depths of up to 4 mm in biological tissues, having a high relative temperature sensitivity of 1.4-1.1% $°C^{-1}$ in the physiological temperature range of 10 - 64 ^oC. These lifetime-based thermosensitive nanoprobes allow for *in vivo* diagnosis of murine inflammation, mapping out the precise temperature distribution profile of nanoprobes-interrogated area.

Keywords: core/shell/shell nanoparticles, lifetime, nanothermometry, NIR II, *in vivo*

1. Introduction

Temperature is a critical factor that governs or affects manifold behaviors of physical, chemical, and biological systems, accurate measurement of which is, therefore, of fundamental importance to unravel the complexity of these systems and to impact a multitude of technological applications ranging from integrated photonic devices to precise medicine[1-3]. Thermocouples and thermistors dominate the market but are inappropriate to probe temperature in live biological systems as physical contact with measured samples is a prerequisite, which disturbs the measurements at sub-millimeter scales[4]. Alternatively, luminescence nanothermometry is emerging as a non-invasive spectroscopic method that allow to probe temperature variation at nanometric spatial resolution and in remote distance, spurring wide interests[5, 6]. The contactless and high-resolution nature makes them ideal candidates for temperature evaluation in the early diagnosis of several diseases as well as for

providing real-time temperature feedback in thermal (hypothermia or hyperthermia) therapies of malignant cancers[7-9].

Indeed, the potential clinical and preclinical applications fuel a fast development of luminescence nanothermometers particularly for *in vivo* studies in the near infrared (NIR) range[10]. Light in the first biological window (NIR-I, 750 - 950 nm) or the second biological window (NIR-II, 1000 - 1700 nm) is known to have minimized scattering and absorption, thus allowing for maximized light penetration depth in tissues [11-13]. Notably, the longer luminescence wavelength in NIR-II than in NIR-I window reduces photon scattering processes in tissue, permitting higher imaging spatial resolution *in vivo*[10]. As a result, different luminescence materials operating in the biological windows (mostly in NIR-II) have been developed, including PbS/CdS/ZnS quantum dots[14], silver sulfide nanoparticles (Ag_2S)[15], rare-earth down-shifting nanoparticles (LaF_3:Nd^{3+}, LaF_3:Nd^{3+}@Yb^{3+}, $NaYF_4$:Yb^{3+}, Ho^{3+}, Er^{3+}, CaF_2:Nd^{3+},Y^{3+})[16-18], rare-earth upconverting nanoparticles ($NaYF_4$:Yb^{3+}/Tm^{3+}, $NaYbF_4$:Tm^{3+})[19, 20], and hybrid luminescent materials[21](Figure 1a). Note that transition metal (manganese) doped colloidal quantum dots using two interconnected emissive excited states[22] and carbon dots using temperature-dependent nonradiative processess[23] have also been described for temprature measurement, but generally in the visible range. These NIR nanothermometers probe temperature fluctuation using luminescence intensity ratio between two emission bands (LIR), peak position (typically from quantum dots), or spectral bandwidth. Tissue-penetrating luminescence enables these nanothermometers for temperature sensing in deep abdomen[24], video-rate recording of subcutaneous thermal alternations[16] [25], and identifying incipient diseases (ischemia or tumors) *in vivo*[25, 26]. However, these demonstrations assume that the spectral profile collected at the detector is identical to the one generated *in situ* by the nanothermometers located in deep tissues.

The optical properties of tissue in-between the nanoparticle probes and the photon detector are often overlooked. Though tissues have low attenuation coefficient in the biological windows, the wavelength-dependent photon absorption and scattering processes still distort the recorded luminescence spectral profile, resulting in inaccurate nanothermometric reading (Figure 1a). *In vivo* experiments demonstrate that these tissue-induced spectral distortions can, indeed, lead to erroneous temperature readings of few degrees[27]. For instance, luminescence spectral profile from nanoparticles codoped with neodymium (Nd^{3+}) and ytterbium (Yb^{3+}) at a fixed temperature (room temperature), after passing through varied thicknesses of biological tissues (chicken breast), were observed to be distorted (Figure 1b, top). As a consequence, the observed LIR between the emission at1050

nm and the emission at 1000 nm, previously established for *in vivo* ratiometric luminescence nanothermometry, is observed to be proportional to the tissue thickness (Figure 1b, bottom; Figure S1), creating artifacts for temperature measurement *in vivo*[28]. Moreover, tissue optical properties vary from tissue type-to-type[11], and are dependent on the felt temperature (Figure 1b), adding complexities to *in vivo* luminescence nanothermometry. Spectral profile deformation demands complicated calibration procedures in order to attain an accurate temperature *in vivo*[27].

Alongside spectral profile, lifetime is a temporal parameter that characterizes the decay process of nanoprobe luminescence, and is independent of nanoprobe concentration and laser irradiance[29-31]. Importantly, luminescence lifetime of nanoprobes remains unaltered after passing through varying thicknesses of biological tissues (Figure 1c), providing possibilities to implement accurate luminescence nanothermometry *in vivo* in the biological windows[32]. Luminescence lifetimes of certain types of carbon dots, quantum dots and organic dyes are temperature-sensitive, but often falling in nanoseconds scale on the same order as that of tissue autofluorescence[21, 30]. Note that in coexistence with high photostability and sharp emission bands, the protection of intra 4f-4f transitions by the outer complete 5s and 5p orbitals make lanthanide luminescence possess have ultralong lifetime on millisecond or sub-millisecond scale, about six orders of magnitude longer than that of tissue autofluorescence[33]. This ultralong lifetime feature enables autofluorescence-free NIR-II lifetime imaging (e.g., at ~ 1000 nm, Figure 1c) in a straightforward way by using commercialized indium gallium arsenide cameras (InGaAs, 950-1700 nm).

Herein, we describe an approach to enable *in vivo* accurate thermographic mapping through thermosensitive lanthanide luminescence lifetime in the NIR-II window. We designed a ternary structure of inert core/active shell/inert shell $NaYF_4$@$NaYF_4$: Yb^{3+}, Nd^{3+} @CaF_2 nanoparticles (tiny size, 13.5 nm), in which thermosensitive ion pairs of neodymium (Nd^{3+}) and ytterbium (Yb^{3+}) ions are incorporated into the thin middle layer (thickness, 1 nm). This architecture allows energy harvesting and utilization within the confined nanoscopic domain, minimizing deactivation processes from both the crystal defects in the core and surface quenching centers. Indeed, the inert core/active shell/inert shell $NaYF_4$@$NaYF_4$: Yb^{3+}, Nd^{3+} @CaF_2 nanoparticles present higher luminescence and longer lifetime than the regular $NaYF_4$: Yb^{3+}, Nd^{3+} @CaF_2 core/ shell structure due to reduced dactivation processes (Figure S2)[34, 35]. Importantly, this ternary structure also places the protected thermoactive domain (the middle layer) close to the probed milieu, thus maximizing the thermosensitivity of the designated nanoprobe.

2. Results and Discussions

Synthesizing ternary domain thermosensitive nanoprobes. A fluorite crystal structure of sodium yttrium fluoride ($NaYF_4$) was adopted to build the inert core/active shell/inert shell $NaYF_4$@$NaYF_4$: Yb^{3+}, Nd^{3+} @CaF_2 nanostructure, in which $NaYF_4$ is known to be one of the most efficient host materials for lanthanide luminescence, having low lattice phonon energy (~ 350 cm^{-1}) that minimizes multiphonon nonradiative processes of excited states[36]. Calcium fluoride (CaF_2) was selected as the outmost inert shell material to shield the optically active middle layer from surface-related quenching processes, as it has high optical transparency range (0.13-10 μm) and low lattice mismatch with $NaYF_4$. Moreover, CaF_2 shell can enhance the nanoprobe biocompatibility, as calcium and fluoride ions are common endogenous components and constituents of calcified tissues like bone and teeth[37]. Nd^{3+} ions are utilized to harvest the excitation light at 800 nm in the NIR-I window, while Yb^{3+} ions act as the lanthanide activators to emit luminescence at ~ 1000 nm in the NIR-II window (Figure 2a). Optical excitation at 800 nm is preferred in *in vivo* experiments as it leads to a minimum thermal loading.[38] Nonradiative energy transfer processes between Nd^{3+} and Yb^{3+} ions, bridging the absorption and the emission process, are responsive to temperature and able to impact observed luminescence lifetimes [16].

A set of ternary domain core/shell/shell nanoparticles designated as $NaYF_4$@$NaYF_4$: Yb^{3+}, Nd^{3+} @CaF_2 with defined amounts of Yb^{3+} and Nd^{3+} dopants were synthesized using a seed-mediated layer-by-layer approach through thermal decomposition of metal trifluoroacetates at high temperature. Nanoparticles of $NaYF_4$ were first used as seeds for the epitaxial growth of the interlayer $NaYF_4$: Yb^{3+}, Nd^{3+}, after which the inert CaF_2 shell was further grown as the outmost protecting layer. Representative transmission electron microscopic (TEM) images of the core $NaYF_4$, the core/shell $NaYF_4$@$NaYF_4$: Yb^{3+}, Nd^{3+}, and the core/shell/shell $NaYF_4$@$NaYF_4$: Yb^{3+}, Nd^{3+} @CaF_2 nanoparticles are shown in Figure 2b, indicative of the near-uniform size and shape for all the resultant samples. Z-contrast high-angle annular dark field scanning TEM (HAADF-STEM) image (Figure 2b, bottom right), which is sensitive to variations in the atomic number of elements in the sample, distinguishes the designated CaF_2 shell (grey) from the $NaYF_4$ host lattice (white), underlying the formation of the desginated core/shell/shell nanoparticles. The size of parent core nanoparticles was measured to be about 6.5 nm, while the size of the core/shell nanoparticles was about 8.5 nm, suggesting the middle layer thickness of ~ 1 nm. Moreover, the size of the resultant core/shell/shell nanoparticles was estimated to be about 13.5 nm, evaluating the

outer CaF_2 layer thickness to be about 2.5 nm (Figure S3), in good agreement with the HAADF-STEM result. Measured x-ray diffraction (XRD) patterns confirmed that the core, the core/shell, and the core/shell/shell nanoaprticles are of the designated fluorite crystal structure (cubic phase) (Figure S4). The pristine ligand of oleic acid on the surface of as-prepared $NaYF_4$@$NaYF_4$: Yb^{3+}, Nd^{3+}@CaF_2 nanoparticles was then substituted by a hydrophilic ligand of poly (acrylic acid) (PAA, MW= 18, 000), converting nanoprobes into aqueous medium for thermosensitivity and thermographic imaging studies. Compared Fourier transform infrared (FTIR) spectra between surface modified nanoparticles and as-prepared nanoparticles (Figure S5) confirm the successful ligand replacement.

Tuning luminescence lifetime thermosensitivity through dopant concentrations. We tuned the thermal sensitivity of luminescence lifetime (at ~ 1000 nm from Yb^{3+} dopant) through varying dopant concentrations of Nd^{3+} and Yb^{3+} ions in the ternary domain $NaYF_4$@$NaYF_4$:Yb^{3+}, Nd^{3+} @CaF_2 nanoparticles. Concentration tuning by Yb^{3+} ions was achieved with a neglible size change or minute size increase for the core/shell (9.4 -11.5 nm) and the core/shell/shell (12.3-13.9 nm) nanoparticles at high Yb^{3+} concentrations (Figure S6). While concentration tuning with Nd^{3+} ions showed no obvious size change of the core/shell and the core/shell/shell nanoparticles (Figure S11). When fixing Nd^{3+} dopant concentration at 50%, variation of Yb^{3+} dopant concentrations (from 2, 5, 10, 20, 30, 40 to 50%) produces pronounced effects on luminescence decay curves of the core/shell and the core/shell/shell nanoparticles at room temperature. Gradual lifetime descending was observed at high Yb^{3+} dopant concentrations in the core/shell $NaYF_4$@$NaYF_4$:Yb^{3+}, Nd^{3+} nanoparticle (Figure S7), being ascribed to the increased surface quenching and surface-related dopant concentration quenching (associated with energy migration process from inside Yb^{3+} ions to surface quenching sites through Yb^{3+} sub-lattice). Shelling $NaYF_4$@$NaYF_4$:Yb^{3+}, Nd^{3+} with inert CaF_2 layer protracted the decay process substantially, and revealed the longest lifetime at Yb^{3+} dopant concentration of 30%, due to the effective alleviation of both surface-related quenching processes. Moreover, all the core/shell/shell samples showed a remarkable temperature-dependent luminescence lifetime at 980 nm (corresponding to the $^2F_{5/2} \rightarrow {}^2F_{7/2}$ transition of Yb^{3+} ions, termed as Yb^{3+} luminescence lifetime below) (Figure S8), while the lifetime at 1060 nm (corresponding to the $^4F_{3/2} \rightarrow {}^4I_{11/2}$ transition of Nd^{3+} ions, termed as Nd^{3+} luminescence lifetime below) (Figure S9) is temperature-independent in a temperature range of 10 - 64 ^oC. This indicates a strong temperature dependence of both $Yb^{3+} \rightarrow Nd^{3+}$ back energy transfer (BET) process and the $Nd^{3+} \rightarrow Yb^{3+}$ energy transfer process that involves phonon assistance (Figure 2e). However, the rates of both processes are supposed to be faster

than or on the same level of the radiative rate of Yb^{3+} luminescence ($1/\tau$, ~ 2,000 s^{-1}) while lower than the radiative rate of Nd^{3+} luminescence ($1/\tau$, ~ 50,000 s^{-1}), thus resulting in a temperature-dependent and -independent luminescence lifetimes for Yb^{3+} and Nd^{3+}, respectively. The Yb^{3+} luminescence lifetime for all the samples was observed to decrease with an increase of temperature (Figure S8). The derivative of Yb^{3+} luminescence lifetime with respect to temperature, *i.e.*, the thermosensitivity, can be evaluated using the following equations[1]:

$$S_a=\left|\frac{d\tau}{dT}\right|, \quad (1)$$

$$S_r=100\%\times\left|\frac{1}{\tau}\frac{d\tau}{dT}\right| \quad (2)$$

Where S_a and S_r represent the absolute and relative temperature sensitivities, respectively; τ and T stand for the luminescence lifetime and the temperature, respectively. For the entire temperature range investigated here, maximum S_r was observed at Yb^{3+} concentration of 20%. And maximum S_a was observed at Yb^{3+} concentration of 20% for temperature below 42 ^oC, while at Yb^{3+}30% for tempeature above 42 ^oC (Figure S10).

The effect of Nd^{3+} dopant concentration on the luminescence lifetime thermosensitivity was also studied in a series of $NaYF_4$@$NaYF_4$: Yb^{3+} 20%, Nd^{3+} x%@CaF_2 core/shell/shell nanoparticles (x= 30, 40, 50, 60, and 80) with a fixed Yb^{3+} dopant concentration of 20%. At room temperature, Nd^{3+} dopant concentration produces negligible effect on the luminescence intensity but pronounced effect on the Yb^{3+} luminescence lifetime, showing a gradual decrease with an elevated Nd^{3+} concentration. This reveals the presence of the $Yb^{3+}\rightarrow Nd^{3+}$ BET process (Figure S12 and Figure 2e). All the samples presented a similar temperature dependence for Yb^{3+} luminescence lifetime, which was shortened at higher temperatures (Figure S13). The Nd^{3+} luminescence lifetime was observed to be virtually temperature-independent for all the Nd^{3+} contents (Figure S14). The relative thermal sensitivity (S_r for Yb^{3+} luminescence lifetime) was shown to ascend when increasing Nd^{3+} concentration from 30 to 60% in the invested temperature range of 10- 65 ^oC (Figure S15). When increasing Nd^{3+} concentration further to 80%, the sample showed a lower S_r than the one with 60% Nd^{3+} in the temperature range of 10-35 ^oC, but higher S_r in the temperature range of 40-65 ^oC. In addition, the sample doped with 80% Nd^{3+} showed the lowest S_a, while the samples doped with 30, 40, and 50% Nd^{3+} present similar S_a in the entire temperature range investigated here. The sample doped with 60% Nd^{3+} showed the highest S_a in the temperature range of 10-20 ^oC, but presented intermediary Sa between the ones of the samples doped with 30, 40, and 50% Nd^{3+} and the lowest one from the 80% Nd^{3+} sample in the temperature of 25-60 ^oC.

As a result, taking both thermal sensitivities and biological applications into consideration, the optimal doping levels for Yb^{3+} and Nd^{3+} in the $NaYF_4$@$NaYF_4$: Yb^{3+}, Nd^{3+}@CaF_2 core/shell/shell nanoparticles were determined to be 20% and 60%, respectively, presenting a sensitive luminescence lifetime to temperature (Figure 2c). An increase of temperature from 10 to 64 °C results in a decrease of lifetime from 898 μs to 450 μs, about 49% decrease. Both S_r and S_a were found to descend with temperature increase in the investigated temperature range (Figure 2d). Importantly, the S_a reaches 13 $\mu s \cdot °C^{-1}$, while Sr reaches as high as 1.4 $\%°C^{-1}$ at 10 °C, about~ 14 fold higher than that of previously reported ratiometric luminescence nanothermometers based on Nd^{3+} and Yb^{3+} ions [16]. We also measured the temperature-dependent spectra of $NaYF_4$@$NaYF_4$: 20%Yb^{3+}, 60%Nd^{3+} @CaF_2 core/shell/shell nanoparticles, the emission intensity of which gradully decreased with an increase of temperature from 10 to 64 °C (Figure S16).

Mechanisms for thermosensitive luminescence lifetime. We performed mechanistic studies to unveil the dependence of Yb^{3+} luminescence lifetime on the temperature and the thermosensitivity on dopant concentrations. The established energy transfer (ET) from Nd^{3+} to Yb^{3+} ions and associated luminescence processes are described in Figure 2e. Heating up $NaYF_4$@$NaYF_4$: Yb^{3+}, Nd^{3+} @CaF_2 nanoparticles (with varied Nd^{3+} or Yb^{3+} concentrations) all result in a temperature-dependent decrease of Yb^{3+} luminescence lifetime (Figures S8 and S13). Depopulation of the emitting $^2F_{5/2}$ sate of Yb^{3+} ions can be caused by two possible processes: One is the multiphonon-assisted nonradiative process[39], while the other one is the BET process from Yb^{3+} to Nd^{3+} ions. Measured Yb^{3+} luminesce lifetime from Yb^{3+}-only $NaYF_4$@ $NaYF_4$: 20% Yb^{3+}@CaF_2 and Nd^{3+} luminesce lifetime from Nd^{3+}-only $NaYF_4$@ $NaYF_4$: 60% Nd^{3+}@CaF_2 nanoparticles remain invariant when elevating temperature, ruling out the first possible process (Figure S17). Observation of Nd^{3+} luminescence when performing direct excitation of Yb^{3+} in $NaYF_4$@$NaYF_4$:Yb^{3+}, Nd^{3+} @CaF_2 nanoparticles confirmed the occurrence of the BET process (Figure S18). Importantly, when coexisting with Nd^{3+} ions, Yb^{3+} luminesce lifetime was observed to be thermosensitive no matter exciting Nd^{3+} dopants at 800 nm (Figure 2c) or Yb^{3+} dopants at 980 nm (Figure 2f), demonstrating the essential role of Nd^{3+}-enacted BET mechanism to regulate the thermal depopulation process of the emitting $^2F_{5/2}$ state of Yb^{3+} ions. Indeed, an elevated temperature can result in a thermal population of higher $^2F_{5/2}$ Stark levels that follow a Boltzmann distribution,[40] minimizing the energy mismatch involved in BET. This minimization favors energy extraction from Yb^{3+} to Nd^{3+} and thus result in temperature-dependent depopulation of the $^2F_{5/2}$ sate of Yb^{3+} ion[41].

The temperature dependence of Yb^{3+} luminescence lifetime is governed by the temperature dependence of both ET and BET rate, the radiative and nonradiative transition (multiphonon process) probabilities, as well as the energy migration (EM) process (among Yb^{3+} ions). As commented before, the luminescence lifetime of Yb^{3+} ions in single doped systems is temperature-independent. This means that the radiative and nonradadiative transition probabilities from the excited state to the ground state of Yb^{3+} are temperature-independent. Energy migration probability is also expected to be temperature independent as it depends on, mainly, the Yb^{3+}-Yb^{3+} distance. Thus, these processes contribute with a temperature-independent background to the luminescence lifetime of Yb^{3+} ions in the presence of energy transfer. In these conditions, the lifetime-based thermal sensitivity would reach a maximum when the BET probability dominates over the other de-excitation mechanisms. Dopant concentrations of Yb^{3+} and Nd^{3+} determine the average ion-ion distances (both Yb^{3+}-Yb^{3+} and Nd^{3+}-Yb^{3+}) in the middle layer of the core/shell/shell nanoparticles that govern both direct and back transfer rates. Low Yb^{3+} concentrations result in long ion distance between Nd^{3+} and Yb^{3+} ions and, thus, lead to a reduction in the BET probabilities. In this situation, temperature independent de-excitation processes are dominant, resulting in a low lifetime thermosensitivity. On the other hand, high Yb^{3+} concentrations lead to shorter ion distances between both Nd^{3+} and Yb^{3+} but also between Yb^{3+} and Yb^{3+} that leads to large EM rates. In this case, again, the BET process is not dominant and the temperature dependence of lifetime decreases. As a result, maximum thermosensitivity is reached for an intermediate Yb^{3+} dopant concentration, which, in our case, has been experimentally determined to be ~ 20%. The same argument applies to explain the improvement of lifetime thermosensitivity with the Nd^{3+} concentration. For a fixed Yb^{3+} concentration, high Nd^{3+} concentrations increase the BET rates making it dominant over the other de-excitation mechanisms and thus leading to an enhancement in the temperature dependence of Yb^{3+} luminescence lifetime (Figure S15b).

Assessment of ternary domain nanoprobes for thermal sensing. We chose the optimized $NaYF_4$@ $NaYF_4$: Yb^{3+}20%, Nd^{3+}60%@CaF_2 nanoprobes to assess their potential use for luminescence lifetime thermal sensing. We first calibrated the Yb^{3+} luminescence lifetime versus temperature in a range of 10- 70 ºC (Figure 3a and 3b). Attained experimental data can be well fitted by the following equation (R^2=0.998):

$$\tau=0.06347T^2-13.0927T+10109.817 \quad (3)$$

where τ is the Yb^{3+} luminescence lifetime (μs) and T is the temperature (ºC).

To pose these nanoprobes for *in vivo* applications, the stability of luminescence lifetime was evaluated against long-term intense laser exposure, thermal hysteresis, nanoprobe concentration, and harsh environment (acid and base). Under continuous wave intense laser irradiance (2 W/cm^2, about 20-fold higher than the one typically used for *in vivo* experiments), the luminescence lifetime of the ternary domain probe remains invariant over 5 hours (Figures 3c and S19a), rendering them possible for long-term biological experiments. Luminescence decay curves of the ternary domain nanoprobe were also measured over five cycles of heating and cooling process between 18 and 41 ^{o}C (Figures 3d and S19b), with an estimated temperature uncertainty of 1.0 ^{o}C at 41 ^{o}C. No thermal hysteresis was observed, demonstrating that the nanoprobe possesses excellent thermal sensing repeatability. Moreover, measured luminescence lifetimes were shown to be identical at varied nanoprobe concentrations (1.25-12.5 mg/ml, water dispersion) (Figures 3c and S19c), and also at a broad range of pH from 1 to 12 (Figures 3f and S19d). It is known that after oral or intravenous administration, nanoparticles can be accumulated *in vivo* in internal organs (such as stomach and liver) due to pharmacokinetic biodistribution, or into malignant tumor sites due to targeting delivery or enhanced permeability and retention (EPR) effect[42]. Microenvironments in the body can also be harsh: The normal pH of the stomach is roughly 1.5 – 2.0, while tumor tissue is featured to have extracellular acidic microenvironment (pH 6.5 – 6.9)[43]. The independence of NIR-II luminescence lifetime versus the nanoprobe concentration and pH values makes them ideal candidates for *in vivo* remote thermal sensing in internal organs.

Thermographic imaging through tissue-mimicking phantom. We performed thermographic imaging of the optimized ternary domain $NaYF_4$@ $NaYF_4$: Yb^{3+}20%, Nd^{3+}60%@CaF_2 nanoprobes (aqueous dispersion, 10 mg/ml) at a set of prefixed temperature and through tissue-mimicking phantom with defined thicknesses. As illustrated in Figure 4a, nanoprobes in a quartz cuvette were placed in between a temperature-controlled heating platform and the tissue phantom with varied thicknesses. A thermocouple was positioned in colloidal solution for temperature control. An NIR-sensitive InGaAs camera was utilized to attain NIR-II lifetime-encoded images, which was synchronized but triggered at a precisely defined delay time to a square-wave pulsed excitation laser (see Methods). We calibrated the luminescence lifetime versus temperature in our home-made NIR time-resolved imaging system through measurement of lifetime-hued images of nanoprobe solution without the coverage of tissue-mimicking phantom. The luminescence lifetime-hued images are homogenous and have a clear relation with temperature increase, presenting temperature-encoded image colour (Figure 4b). The attained lifetime thermographic results are in good

accordance with the result measured through a thermal camera (Figure S20). Also, we measured lifetime-hued thermographic images of nanoprobes through intralipid (1%) medium, an established tissue-mimicking phantom, of varying thicknesses (2-4 mm). Although luminescence intensity images are depth-dependent (Figure S21), lifetime-hued thermographic images can be consistently resolved through varied thickness (2, 3, and 4 mm) and at a set of temperatures (30, 35, 40, and 45 ^{o}C) (Figure 4c). The independence of thermal readout on the tissue phantom thickness constitutes the advantage of lifetime-based thermal sensing over spectral-based alternatives, forming a solid prerequisite for reliable thermal sensing at the preclinical level.

Thermographic imaging *in vivo.* We then utilized the thermosensitive ternary domain nanoprobes to image temperature distribution in living mice. An inflammation in mouse is often accompanied by an increase of body temperature[44, 45]. In order to demonstrate the ability of our nanoprobes for accurate thermal monitoring of inflammation we injected the 10% yeast solution (100 μl) into the back of one Kunming mouse to induce an inflammatory mouse. For control purpose we also injected an aliquot of normal saline to the other Kunming mouse. A subcutaneous injection of ternary domain nanoprobes (100 μl, 10 mg/ ml) was also applied to the back of the two mice. 16 h post injection, NIR-II luminescence images clearly show the presence of the thermosensitive nanoprobes inside the inflamed and normal mouse (Figure 5a). At this post-injection time the thermal images of the two mice were acquired with a thermal camera (Figure 5b). Thermal images reveal a slight (≈ 2.6 ºC) increment in skin temperature in the mouse subjected to the yeast solution administration. Time gating methodology was then adopted to obtain the luminescence lifetime images of both mice using the setup in Figure 4a. The resulting images in the time domain are shown in Figure 5c. Note that in the mouse subjected to the yeast injection the lifetime of thermosensitive ternary domain nanoprobes was evaluated, on average, to be 0.68 ms, while in the control mouse the average lifetime was calculated to be 0.70 ms. This constitutes a 2.8% reduction in the lifetime, in correlation with an increment in the subcutaneous temperature. According to the thermal sensitivity of the nanoprobes (1.2 %/ºC) this lifetime reduction is associated with a temperature increment of 2.3 ºC, in good agreement with the temperature change acquired through the thermal camera. This is reasonable as the position of probed subcutis is close to skin, resulting in close skin temperature (the one measured with the thermal camera) and subcutaneous temperature. Note that the acquired temporal luminescence lifetime images are also able to present the precise temperature distribution profile in the nanoprobes-interrogated area.

3. Conclusions

In summary, we describe a class of ternary domain $NaYF_4$@ $NaYF_4$:Yb^{3+}, Nd^{3+}@CaF_2 inert core/active shell/inert shell nanoprobes with a tiny size of ~ 13.5 nm, in which NIR-II luminescence lifetime at 1000 nm (from Yb^{3+}) is sensitive to temperature. This structure confines the thermosensitive lanthanide ion pair to the middle layer, being close to the surrounding environment while shielding deleterious effects from both the core and the surrounding environment. We revealed that both Nd^{3+} and Yb^{3+} concentrations play an important role in tuning nanoprobe temperature sensitivity, through regulation of the temperature-dependent back energy transfer process from Yb^{3+} to Nd^{3+} ions and the energy migration process between Yb^{3+} and Yb^{3+} ions. The luminescence lifetime thermosensitive nanoprobes were shown to be stable against intense laser exposure, independent of nanoprobe concentration, having reliable repeatability, and being able to work in harsh environment with pH ranging from 1 to12. Importantly, the nanoprobes are able to probe precise temperature at varied tissue depths and allow an accurate thermographic mapping of temperature distribution in nanoparticles-probed area *in vivo*. These superior advantages render the described nanoprobes as ideal nanothermometers for temperature measurement in live mammals.

4. Experimental Section

Materials: Rare-earth oxides Er_2O_3, Y_2O_3, and Yb_2O_3, sodium trifluoroacetate (NaTFA), and trifluoroacetic acid (TFA) were purchased from Aladdin Chemistry Co. Ltd. Oleic acid (OA, >90%), oleylamine (OM, >70%), and 1- octadecence (ODE, >90%) were obtained from Sigma-Aldrich Co. Ltd. Hexane and ethanol were purchased from Beijing Chemical Reagents, China. All materials were used as received without further purification.

Synthesis of α-$NaYF_4$ core nanoparticles: The α-$NaYF_4$ nanoparticles without lanthanide doping were prepared via thermal decomposition of sodium and yttrium trifluoroacetates at high temperatures. First, 0.5 mmol Y_2O_3 were completely dissolved in 10 ml trifluoroacetatic acid (TFA) at an elevated temperature (90 ^oC) in a three-neck flask. Then, evaporation of the solution under argon purge yielded solid $Y(TFA)_3$ powder, which was further dissolved in a mixture solution comprising OA (3.2 ml), OM (3.2 ml), ODE (6.4 ml) and NaTFA (1 mmol). Susequently, the solution was heated to 110 ^oC and kept at this temperature for 30 min, and then to 310 ^oC for 30 min before naturally cooling down to room temperature. The resultant core nanoparticles were collected with centrifuation (6000 rpm for 5 min, after adding 20ml

ethanol), washed with ethanol (three times), and finally dispersed in 10 ml hexane for further uses.

Synthesis of α-$NaYF_4$@ $NaYF_4$: Yb^{3+} x%, Nd^{3+} 50% (x=2, 5, 10, 20, 30, 40, and 50) core/shell nanoparticles: The core/shell nanoparticles were prepared following a seed-mediated epitaxial growth procedure using the as-prepared α -$NaYF_4$ as the core nanoparticles. The Re $(TFA)_3$ shell precursors were first synthesized using the identical procedure as that for the preparation of $Y(TFA)_3$ precursor, except that x mmol Yb_2O_3 (x=0.01, 0.25, 0.05, 0.1, 0.15, 0.2, and 0.25), 0.25 mmol Nd_2O_3, and (0.25-x) mmol Y_2O_3 were used. Second, the Re $(TFA)_3$ shell precursors were mixed with 10 ml OA, 10 ml ODE, 0.5 mmol NaTFA, and 0.5 mmol core nanoparticles in a three-neck flask. The solution was then heated to 120 ^oC for 30 min, and further to 300 ^oC for 30 min before a natural cooling down to room temperature. The resultant core/shell nanoparticles were collected following the identical procedure as that for collecting the α-$NaYF_4$ core nanoparticles, and also dispersed in in 10 ml hexane for further uses.

Synthesis of α-$NaYF_4$@$NaYF_4$: Yb^{3+} x%, Nd^{3+} 50% (x=2, 5, 10, 20, 30, 40, and 50) @CaF_2 core/ shell/ shell nanoparticles: The procedure for the preparation of the core/shell/shell nanoparticles is similar to the one for preparing the α-$NaYF_4$@ $NaYF_4$: Yb^{3+} x%, Nd^{3+} 50% core/shell nanoparticles. Instead, the α-$NaYF_4$@$NaYF_4$: Yb^{3+}, Nd^{3+} core/shell nanoparticles were used to subsitute the α-$NaYF_4$ particles for a seed-mediated growth of the shell. In brief, a mixture of α-$NaYF_4$@$NaYF_4$: Yb^{3+}, Nd^{3+} core/shell nanoparticles (5 mL, hexane dispersion), 7 ml OA, and 7 ml ODE were first heated to 310 ^oC and maintained at this temperature under argon gas protection. Subsequently, the Ca-TFA-OA (0.5 mmol/ml, 1.6 ml) shell precursors were injected into the solution for two times with an interval of about 25 min. The resultant core/shell/shell nanoparticles were precipitated, washed with ethanol, and finally dispersed in 10 mL hexane.

Synthesis of α-$NaYF_4$@ $NaYF_4$: Yb^{3+}20%, Nd^{3+} x% (x= 30, 40, 50, 60, and 80) core/shell nanoparticles: The synthesis procedure of α-$NaYF_4$@ $NaYF_4$: Yb^{3+}20%, Nd^{3+} x% (x= 30, 40, 50, 60, 80) is identical to that used for the preparation of α-$NaYF_4$@$NaYF_4$: Yb^{3+} x%, Nd^{3+}50% (x=2, 5, 10, 20, 30, 40, 50), except for different amounts of rare-earth oxides.

Synthesis of α-$NaYF_4$@ $NaYF_4$: Yb^{3+} 20%, Nd^{3+} x% (x= 30, 40, 50, 60, and 80) @CaF_2 core/shell/shell nanoparticles: The synthesis procedure of α-$NaYF_4$@ $NaYF_4$: Yb^{3+} 20%, Nd^{3+} x% (x= 30, 40, 50, 60, 80) @CaF_2 is identical to that used for the preparation of α-$NaYF_4$@$NaYF_4$: Yb^{3+} x%, Nd^{3+}50% (x=2, 5, 10, 20, 30, 40, 50) @CaF_2.

Preparation of aqueous ternary-domain nanoprobes: First, 2 ml ternary domain $NaYF_4$@ $NaYF_4$: Yb^{3+}, Nd^{3+} @CaF_2 nanoparticles dispersed in hexane were added to 5 ml N, N-dimethylformamide (DMF) solution of nitrosonium tetrafluoroborate ($NOBF_4$) at room temperature. The mixture was then gently shaken until precipitation of nanoparticles was observed. Subsequently, 10 ml toluene and 10 ml hexane were added, and the mixture was centrifuged at 8000 rpm for 10 minutes. The precipitate was collected and dispersed in 5 ml DMF. Next, 280 mg poly (acrylic acid) (PAA) (MW = 18,000) was added to the DMF solution, which was then heated to 80 ° C for 30 minutes with vigorous stirring. Thereafter, the resultant nanoprobes were precipitated by adding acetone, and finally dispersed in purified water.

Animal experiments: Female Kunming mice were purchased from The Second Affiliated Hospital of Harbin Medical University. The animal procedures were in accordance with the guidelines of the Institutional Animal Care and Use Committee, Harbin Institute of Technology. The inflammatory model was established by injecting 10% yeast on the back of the mouse (10 ml/kg), and the same volume normal saline was injected to another mouse as a control [46]. The temperature of the mice was monitored by the infrared thermal camera (Fotric 280s, Shanghai, China) every one hour, and after 16 hours, the luminescence lifetime-encoded images were collected.

Lifetime imaging and decoding. Optical excitation was performed using a fiber-coupled 800 nm laser diode, which run at 1 Hz and with a 40% duty cycle and delivered an averge power density of 50 mW/cm^2. The luminescence images were collected by an NIR-II InGaAs camera (C-Red 2), which was synchronized with the excitation laser at triggered at a precisely defined delay time. The camera kept for integration before the arrival of next laser pulse. A series of time delays were set to sample separate sections of the luminescence decay curve of the nanoprobe. For each pixel of the luminescence lifetime image, the lifetime was fitted by the equation, $I_t=I_0\times e^{-t/\tau}$, where t is delay time, I_0 is the luminescence intensity at t=0, τ is

the lifetime of the nanoprobes. All the image processing was carried out in the commcercialized MATLAB software.

Supporting Information

Supporting Information is available from the Wiley Online Library or from the author.

Acknowledgements

This work was supported by the grants from the National Natural Science Foundation of China (51972084 and 51672061).

Author contributions

The idea and experiments were conceived and designed by M. T. and G. C.. The manuscript was written by M. T. and G.C., and edited by N. C. and D. J.. All experiments were performed by M. T. and F. L., and all authors contributed to the data analysis and interpretation. This work was completed under the supervision of G. C..

Competing interests

The authors declare no competing financial interests.

Received: ((will be filled in by the editorial staff))
Revised: ((will be filled in by the editorial staff))
Published online: ((will be filled in by the editorial staff))

References

[1] C. D. Brites, P. P. Lima, N. J. Silva, A. Millán, V. S. Amaral, F. Palacio ,L. D. Carlos, *Nanoscale* **2012,** *4*, 4799.

[2] D. Jaque ,F. Vetrone, *Nanoscale* **2012,** *4*, 4301.

[3] X. D. Wang, O. S. Wolfbeis ,R. J. Meier, *Chem. Soc. Rev.* **2013,** *42*, 7834.

[4] C. D. Brites, K. Fiaczyk, J. F. Ramalho, M. Sójka, L. D. Carlos ,E. Zych, *Advanced Opt. Mater.* **2018,** *6*, 1701318.

[5] W. W. W. Hsiao, Y. Y. Hui, P. C. Tsai ,H. C. Chang, *Acc. Chem. Res.* **2016,** *49*, 400.

[6] T. Bai ,N. Gu, *Small* **2016,** *12*, 4590.

[7] X. Zhu, W. Feng, J. Chang, Y. W. Tan, J. Li, M. Chen, Y. Sun ,F. Li, *Nature Commun.* **2016,** *7*, 10437.

[8] E. Carrasco, B. del Rosal, F. Sanz‐Rodríguez, Á. J. de la Fuente, P. H. Gonzalez, U. Rocha, K. U. Kumar, C. Jacinto, J. G. Solé ,D. Jaque, *Adv. Funct. Mater.* **2015,** *25*, 615.

[9] B. del Rosal, E. Carrasco, F. Ren, A. Benayas, F. Vetrone, F. Sanz‐Rodríguez, D. Ma, Á. Juarranz ,D. Jaque, *Adv. Funct. Mater.* **2016,** *26*, 6060.

[10] B. del Rosal, E. Ximendes, U. Rocha ,D. Jaque, *Adv. Opt. Mater.* **2017,** *5*, 1600508.

[11] A. Bashkatov, E. Genina, V. Kochubey ,V. Tuchin, *J. Phys. D: Appl. Phys.* **2005,** *38*, 2543.

[12] R. Wang, X. Li, L. Zhou ,F. Zhang, *Angew. Chem. Int. Ed.* **2014,** *53*, 12086.

[13] A. Bashkatov, E. Genina, V. Kochubey ,V. Tuchin, *Opt. Spectrosc.* **2005,** *99*, 836.

[14] A. Benayas, F. Ren, E. Carrasco, V. Marzal, B. del Rosal, B. A. Gonfa, Á. Juarranz, F. Sanz‐Rodríguez, D. Jaque ,J. García Solé, *Adv. Funct. Mater.* **2015,** *25*, 6650.

[15] B. del Rosal, D. Ruiz, I. Chaves Coira, B. H. Juárez, L. Monge, G. Hong, N. Fernández ,D. Jaque, *Adv. Funct. Mater.* **2018,** *28*, 1806088.

[16] E. C. Ximendes, W. Q. Santos, U. s. Rocha, U. K. Kagola, F. Sanz-Rodríguez, N. Fernández, A. d. S. Gouveia-Neto, D. Bravo, A. M. Domingo ,B. del Rosal, *Nano Lett.* **2016,** *16*, 1695.

[17] M. Kamimura, T. Matsumoto, S. Suyari, M. Umezawa ,K. Soga, *J. Mater. Chem. B* **2017,** *5*, 1917.

[18] M. Quintanilla, I. García, I. de Lázaro, R. García-Alvarez, M. Henriksen-Lacey, S. Vranic, K. Kostarelos ,L. M. Liz-Marzán, *Theranostics* **2019,** *9*, 7298.

[19] R. Wu, J. Zhou, L. Lei, S. Zhang, Z. Xiao, J. Zhang ,S. Xu, *Chem. Phys. Lett.* **2017,** *667*, 206.

[20] X. Wang, J. Zheng, Y. Xuan ,X. Yan, *Opt. Exp.* **2013,** *21*, 21596.

[21] E. N. Cerón, D. H. Ortgies, B. del Rosal, F. Ren, A. Benayas, F. Vetrone, D. Ma, F. Sanz Rodríguez, J. G. Solé ,D. Jaque, *Adv. Mater.* **2015,** *27*, 4781.

[22] V. A. Vlaskin, N. Janssen, J. van Rijssel, R. Beaulac ,D. R. Gamelin, *Nano Lett.* **2010,** *10*, 3670.

[23] S. Kalytchuk, K. i. Poláková, Y. Wang, J. P. Froning, K. Cepe, A. L. Rogach ,R. Zbořil, *ACS Nano* **2017,** *11*, 1432.

[24] S. Sekiyama, M. Umezawa, S. Kuraoka, T. Ube, M. Kamimura ,K. Soga, *Sci. Rep.* **2018,** *8*, 1.

[25] H. D. Santos, E. C. Ximendes, M. d. C. Iglesias de la Cruz, I. Chaves Coira, B. del Rosal, C. Jacinto, L. Monge, I. Rubia Rodríguez, D. Ortega ,S. Mateos, *Adv. Funct. Mater.* **2018,** *28*, 1803924.

[26] E. C. Ximendes, U. Rocha, B. Del Rosal, A. Vaquero, F. Sanz Rodríguez, L. Monge, F. Ren, F. Vetrone, D. Ma ,J. García Solé, *Adv. Health. Mater.* **2017,** *6*, 1601195.

[27] Y. Shen, J. Lifante, N. Fernández, D. Jaque ,E. Ximendes, *ACS Nano* **2020,** *14*, 4122.

[28] X. Qiu, Q. Zhou, X. Zhu, Z. Wu, W. Feng ,F. Li, *Nature Commun.* **2020,** *11*, 1.

[29] H. Itoh, S. Arai, T. Sudhaharan, S.-C. Lee, Y.-T. Chang, S. i. Ishiwata, M. Suzuki ,E. B. Lane, *Chem. Commun.* **2016,** *52*, 4458.

[30] P. Haro González, L. Martínez Maestro, I. Martín, J. García Solé ,D. Jaque, *Small* **2012,** *8*, 2652.

[31] Z. Ji, Y. Cheng, X. Cui, H. Lin, J. Xu ,Y. Wang, *Inorg. Chem. Front.* **2019,** *6*, 110.

[32] T. Chihara, M. Umezawa, K. Miyata, S. Sekiyama, N. Hosokawa, K. Okubo, M. Kamimura ,K. Soga, *Sci. Rep.* **2019,** *9*, 1.

[33] Q. Ma, J. Wang, Z. Li, X. Lv, L. Liang ,Q. Yuan, *Small* **2019,** *15*, 1804969.

[34] R. Wu, L. Lei, S. Zhang, Z. Xiao, J. Zhang ,S. Xu, *J. Mater. Chem. C* **2016,** *4*, 9183.

[35] Z. Li, W. Park, G. Zorzetto, J. S. Lemaire ,C. Summers, *Chem. Mater.* **2014,** *26*, 1770.

[36] G. Chen, H. Qiu, P. N. Prasad ,X. Chen, *Chem. Rev.* **2014,** *114*, 5161.

[37] Y. F. Wang, L. D. Sun, J. W. Xiao, W. Feng, J. C. Zhou, J. Shen ,C. H. Yan, *Chem. Eur. J.* **2012,** *18*, 5558.

[38] L. M. Maestro, P. Haro González, B. Del Rosal, J. Ramiro, A. Caamano, E. Carrasco, A. Juarranz, F. Sanz Rodríguez, J. G. Solé ,D. Jaque, *Nanoscale* **2013,** *5*, 7882.

[39] L. H. Fischer, G. S. Harms ,O. S. Wolfbeis, *Angew. Chem. Int. Ed.* **2011,** *50*, 4546.

[40] A. Bednarkiewicz, M. Stefanski, R. Tomala, D. Hreniak ,W. Strek, *Phys. Chem. Chem. Phys.* **2015,** *17*, 24315.

[41] D. Jaque, M. Ramirez, L. Bausá, J. G. Solé, E. Cavalli, A. Speghini ,M. Bettinelli, *Phys. Rev. B* **2003,** *68*, 035118.

[42] J. K. Patra, G. Das, L. F. Fraceto, E. V. R. Campos, M. del Pilar Rodriguez Torres, L. S. Acosta Torres, L. A. Diaz Torres, R. Grillo, M. K. Swamy ,S. Sharma, *J. Nanobiotechnology* **2018,** *16*, 71.

[43] X. Zhang, Y. Lin ,R. J. Gillies, *J. Nucl. Med.* **2010,** *51*, 1167.

[44] M. Brenner, C. Braun, M. Oster ,P. S. Gulko, *Ann. Rheu. Dis.* **2006,** *65*, 306.

[45] B. M. Sanchez, M. Lesch, D. Brammer, S. E. Bove, M. Thiel ,K. S. Kilgore, *J. Pharmacol. Toxicol.* **2008,** *57*, 169.

[46] C. Van Arman, A. Begany, L. Miller ,H. Pless, *J. Pharmacol. Exp. Ther*. **1965,** *150*, 328.

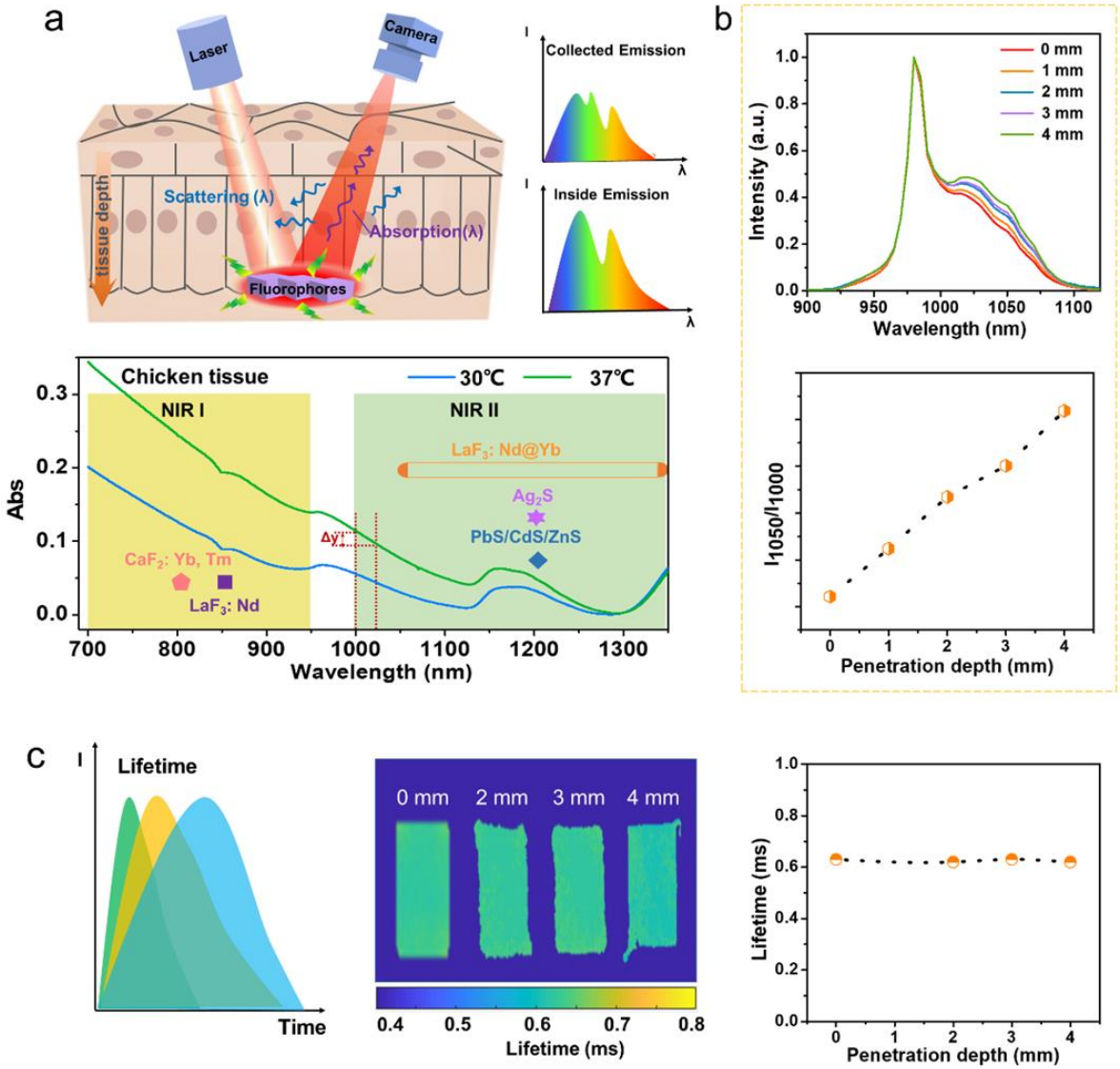

Figure 1. Luminescence nanothermometers in the near infrared range. a. A schematic illustration of thermographic luminescence imaging through biological issues (top); the absorbance of biological tissue (chicken breast) at two different temperatures between 700-1350 nm marked with reported nanothermometers in both the NIR-I and NIR-II biological windows[14-16, 19]. **b.** Normalized luminescence spectra of ternary domain $NaYF_4$@ $NaYF_4$:Yb^{3+}, Nd^{3+}@CaF_2 nanoparticles through varying depth of chicken tissue (top), and luminescence intensity ratio between 1050 nm and 1000 nm plotted against tissue depth (bottom). **c.** A schematic illustration of luminescence decay process in the time domain (left), luminescence lifetime imaging of NIR-emitting nanoparticles, exemplified here by ternary domain $NaYF_4$@ $NaYF_4$:Yb^{3+}, Nd^{3+}@CaF_2 at 1000 nm, through varying depth of biological tissue (middle), and the extracted lifetime value plotted against tissue depth (right).

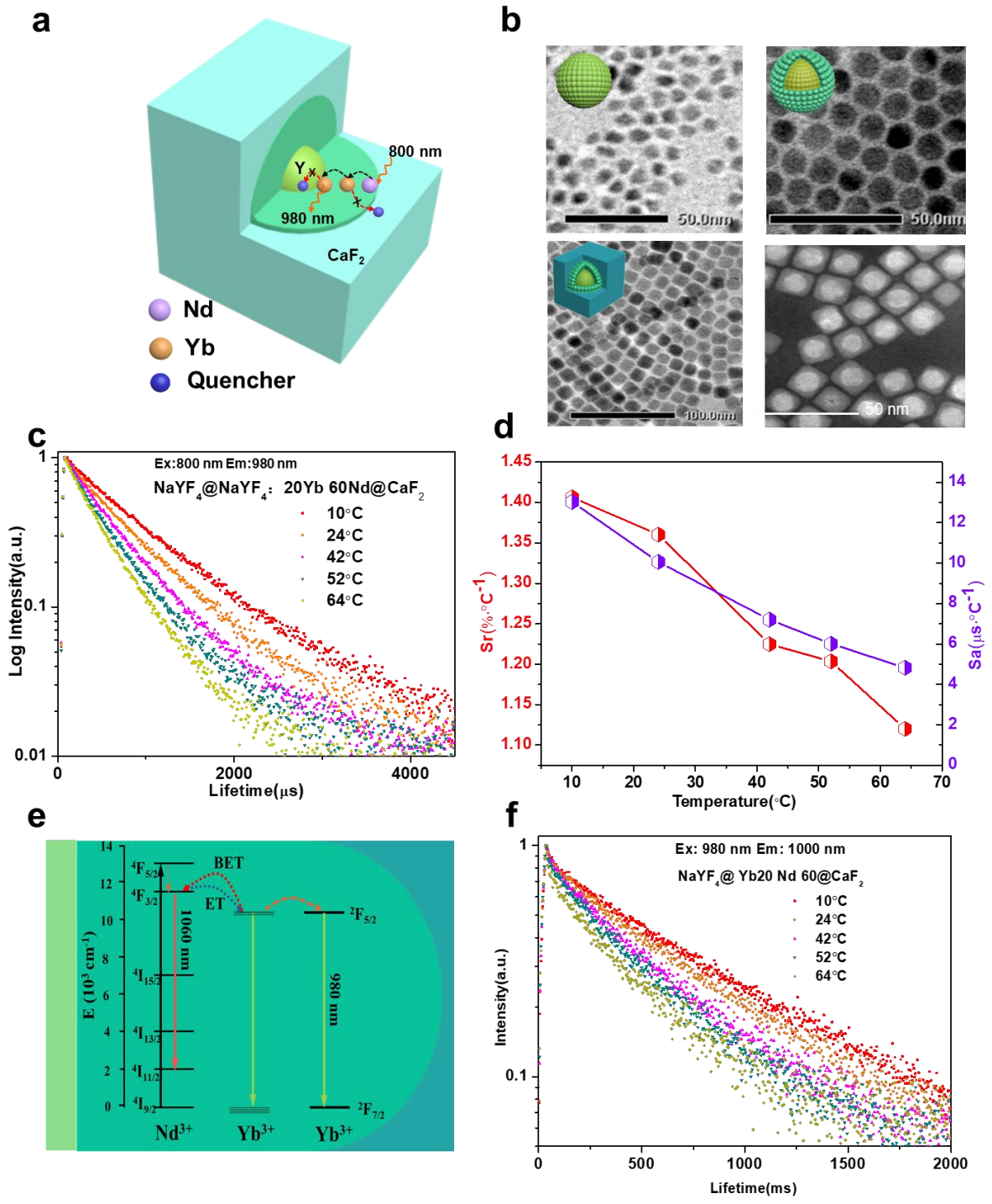

Figure 2. Ternary domain thermosensitive nanoprobe for luminescence lifetime-based temperature measurement. a. An illustration of the designated ternary domain inert core/active shell/inert shell structure, in which thermosensitive lanthanide ion pairs are incorporated into the middle layer to ensure being close to probed environment while preventing detrimental effects from both the inner core and the surrounding environment. **b.** Representative transmission electron microscopy (TEM) images of the core $NaYF_4$(top left), the core/shell $NaYF_4$@ $NaYF_4$:Yb^{3+}, Nd^{3+} (top right), and the core/shell/shell $NaYF_4$@

$NaYF_4$: Yb^{3+}, Nd^{3+}@CaF_2 (bottom left), along with a HAADF STEM image of the core/shell/shell $NaYF_4$@ $NaYF_4$: Yb^{3+}, Nd^{3+}@CaF_2 (bottom right). **c.** Measured temperature-dependent Yb^{3+} luminescence lifetime in the optimized ternary domain $NaYF_4$@ $NaYF_4$: 20% Yb^{3+}, 60% Nd^{3+}@CaF_2 nanoprobe under photoexcitation of Nd^{3+} at 800 nm. **d.** Absolute sensitivity (S_a) and relative thermal sensitivity (S_r) plotted against temperature in a physiological range of 10 - 64 ºC for the optimized ternary domain nanoprobe. **e.** A simplified energy levels of Nd^{3+} and Yb^{3+} ions illustrating the excitation (solid black line), the energy transfer processes (dashed line), and the luminescence process (solid red or yellow line). **f.** Measured temperature-dependent Yb^{3+} luminescence lifetime in the optimized ternary domain nanoprobe under direct photoexcitation of Yb^{3+} at 980 nm.

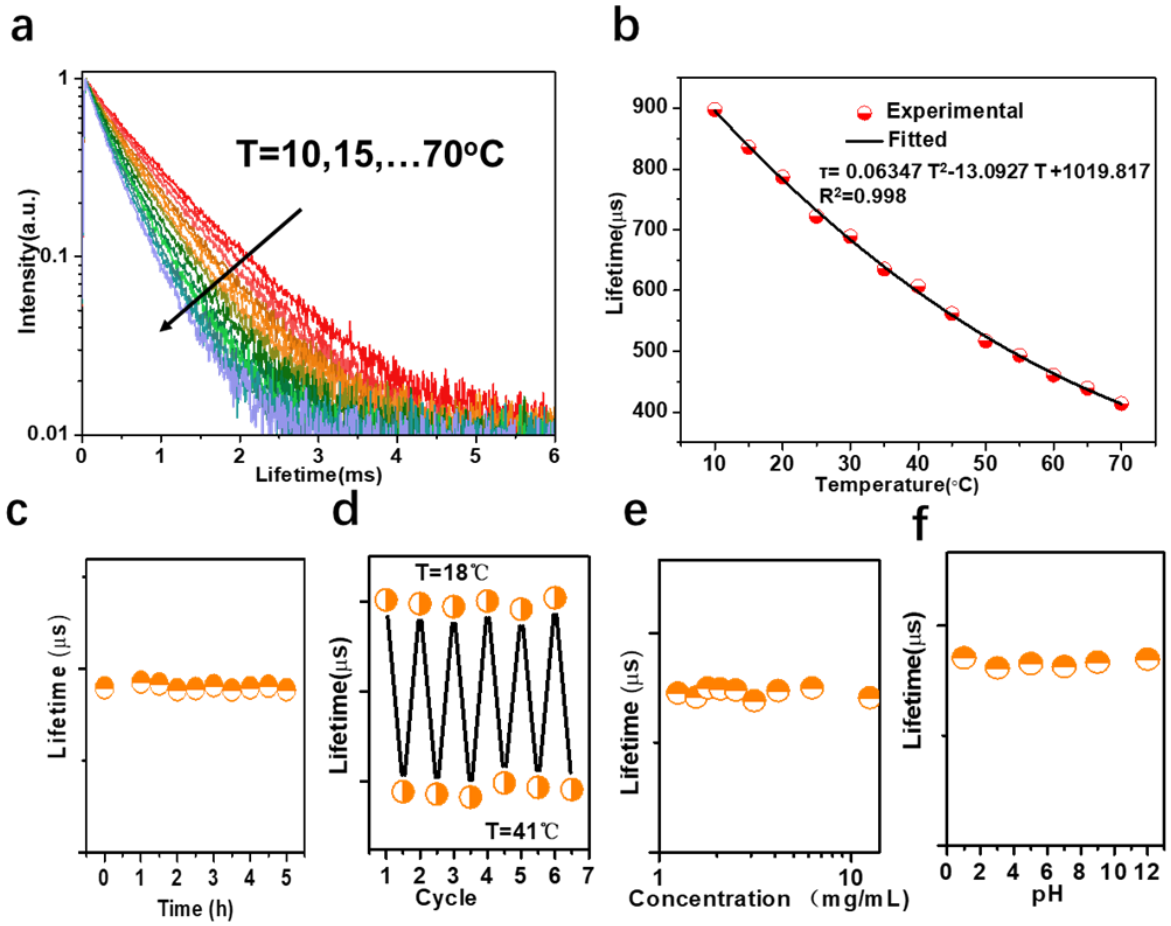

Figure 3. Assessment of the ternary domain thermosensitive nanoprobes. a. Measured temperature-dependent luminescence lifetime of the ternary domain nanoprobe at different temperatures. **b.** A calibration curve between measured lifetime and temperature with a good nonlinear fitting in the range of 10-70 °C. **c.** Stability of luminescence lifetime against intense laser exposure (at 800 nm) over 5 h at 24 °C. **d.** Repeatability of luminescence lifetime over five cycles of heating and cooling between 18 and 41 °C. **e.** Measured luminescence lifetime versus nanoprobes concentration at 24 °C. **f.** Stability of luminescence lifetime in harsh environment with pH varying from 1 and 12 at 24 °C.

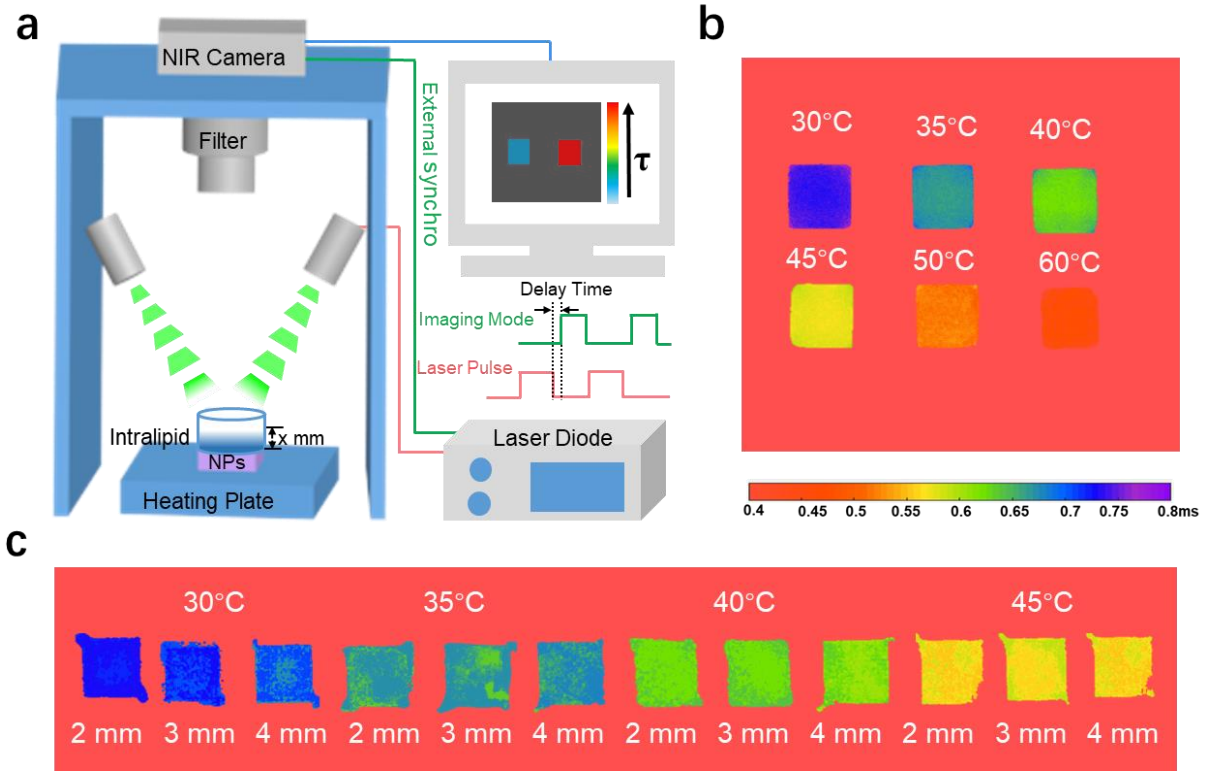

Figure 4. Thermographic imaging through tissue-mimicking phantom. a. An illustration of home-made time-resolved imaging system to acquire luminescence lifetime image of the optimized $NaYF_4$@ $NaYF_4$: Yb^{3+}20%, Nd^{3+}60%@CaF_2 nanoprobes with defined temperature through intralipid (1%) medium at a depth of x mm (x = 0, 1, 2, 3 and 4). The purple cuboid marks the nanoparticles contained in a cuvette. **b.** Thermographic luminescence lifetime imaging of the optimized ternary domain nanoprobes at defined temperature between 30 and 60 ^{o}C. **c.** Thermographic luminescence lifetime imaging of the optimized ternary domain nanoprobes at defined temperature between 30 and 45 ^{o}C and through varying tissue thicknesses of 2 mm, 3 mm, and 4 mm.

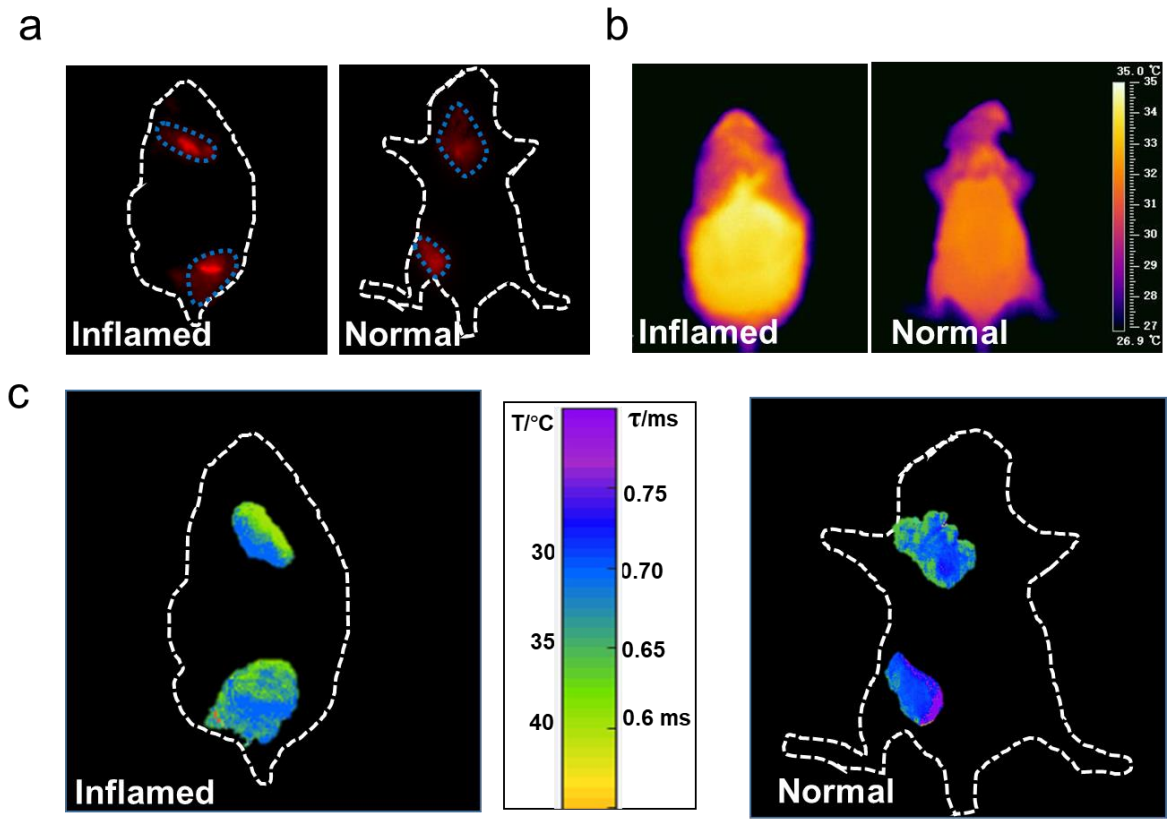

Figure 5. Thermographic imaging of the ternary domain thermosensitive nanoprobes in living mouse. a. Luminescence intensity imaging of the optimized ternary domain $NaYF_4$@ $NaYF_4$: Yb^{3+}20%, Nd^{3+}60%@CaF_2 thermosensitive nanoprobes in the inflamed and normal mouse (The blue dotted line indicates the injection location of the nanoprobes), revealing nanoprobe distribution inside the body (Excitation at ~ 800 nm, integration time 100 ms, 1000 nm band-pass filter). **b.** Captured thermal camera images of the inflamed and normal mouses. **c.** Thermographic luminescence lifetime-hued imaging of the optimized nanoprobes in the inflamed and normal mouses, revealing the precise local temperature distribution surrounding the nanoprobes.

The table of contents entry

A class of $NaYF_4$@ $NaYF_4$: Yb, Nd@CaF_2 lifetime nanothermometers were developed with a high relative temperature sensitivity of 1.4% $°C^{-1}$ in the physiological temperature range of 10 - 64 ^oC. These nanothermometers are able to map out the precise temperature distribution profile of nanoprobes-interrogated area for *in vivo* diagnosis of murine inflammation.

Keyword: core/shell/shell nanoparticles, lifetime, nanothermometry, NIR II, *in vivo*

Meiling Tan[1,2,3], Feng Li[1,2,3], Hui Li[1,2,3], Xin Wang[1,2,3], Chenyang Zhang[1,2,3], Daniel Jaque,[4] and Guanying Chen[1,2,3]*

Title: Accurate *in vivo* nanothermometry through NIR-II lanthanide luminescence lifetime

TOC figure